Hindawi Publishing Corporation
Journal of Control Science and Engineering
Volume 2011, Article ID 594086, 15 pages
doi:10.1155/2011/594086

Research Article

Real-Time Fixed-Order Lateral H_2 Controller for Micro Air Vehicle

Meenakshi M.[1] and M. Seetharama Bhat[2]

[1] *Department of Instrumentation Technology, Dr. Ambedkar Institute of Technology (AIT), Bangalore 560056, India*
[2] *Department of Aerospace Engineering, Indian Institute of Science, Bangalore 560012, India*

Correspondence should be addressed to Meenakshi M., meenakshi_mbhat@yahoo.com

Received 26 April 2011; Accepted 6 September 2011

Academic Editor: Onur Toker

This paper presents the design and development of a fixed low-order, robust H_2 controller for a micro air vehicle (MAV) named Sarika-2. The controller synthesis uses strengthened discrete optimal projection equations and frequency-dependent performance index to achieve robust performance and stability. A single fixed gain low-order dynamic controller provides simultaneous stabilization, disturbance rejection, and sensor noise attenuation over the entire flight speed range of 16 m/sec to 26 m/sec. Comparative study indicates that the low-order H_2-controller achieves robust performance levels similar to that of full order controller. Subsequently, the controller is implemented on a digital signal processor-based flight computer and is validated through the real time hardware in loop simulation. The responses obtained with hardware in loop simulation compares well with those obtained from the offline simulation.

1. Introduction

A Low-cost, remotely piloted MAV named Sarika-2 [1, 2] is designed and built at the Indian Institute of Science, Bangalore, India, for validating modern robust optimal control algorithms. Sarika-2 (shown in Figure 1) is a lightweight (less than 2 kg at take off) and low inertia vehicle. The radio controlled flying of such a low inertia vehicle through joystick-driven manual command is difficult, if not impossible, even under moderate gusty conditions. The radio-controlled flying becomes easier with the fast damped response of a controlled airframe [3].

Though conventional flight control design methods have been in practice for a long time, such methods suffer from known limitations. They are time consuming. Controller tuning for multi-input multi-output (MIMO) systems is also not straightforward. Another serious limitation of a conventional controller is its poor robustness against model uncertainty. The quest for robust controllers in the last three decades resulted in controllers [4–7] which robustly stabilize the system, leaving the impression that such methods lean too heavily on robustness and sacrifice an adequate view of performance. The H_2 performance level of a plant is often a more realistic indication of its real-life performance [8–10] as compared to the more conservative H_∞-norm [4–7]. Robust H_2 controllers as well as other robust controllers like μ [11] and H_∞ [4–7] provide systematic procedures for obtaining controllers that meet performance objectives and guaranteed robustness against model uncertainty and unmeasured disturbances. In μ synthesis, H_2 and H_∞ loop shaping, the designer specifies frequency-dependent weights [4] to reflect the desired performance and robustness objectives. However, these techniques give controllers, order of which is normally higher than that of a given plant. Hence, real-time controller implementation is hard if not impossible. Implementation of large-order controllers may create undesirable time delays. Therefore, a robust fixed-order H_2 control is an attractive option among the several robust multivariable methods for controller design, since the H_2 norm is the more intuitive measure of the performance [8, 10]. Fixed low-order H_2 controller can be synthesized in one step in contrast to the other multivariable robust

Figure 1: Microair vehicle: Sarika-2.

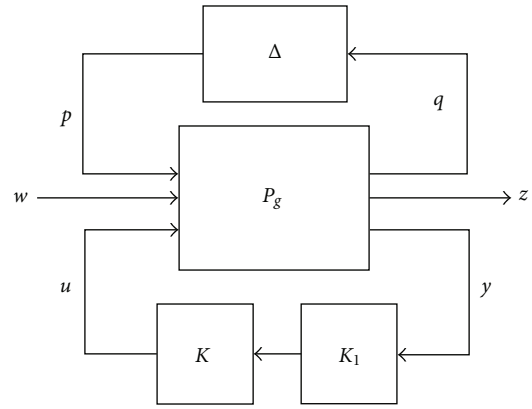

Figure 2: Standard representation for H_2 design and analysis.

controller design methods involving two-step designs [12]. A single-step procedure guarantees the stability robustness and optimality [13].

Robust H_2 optimal controller problem can be posed as H_2 optimal control problem, where in the model uncertainties are accommodated in the design. Thus in contrast to the LQG design, where the estimation of performance and robustness of the closed-loop system is posterior of the controller design and the performance and robustness specifications are included in H_2 controller at the design stage itself. A standard robust H_2 optimization problem can be represented as shown in Figure 2 [3], where attenuation system is subjected to noise and disturbances. The configuration shown in Figure 2 contains a generalized plant that is used for robust stability analysis and controller design.

The signals "w" and "z" are exogenous inputs and performance variables respectively. "y" is the measured variable, and "u" is the control input. P_g is the generalized plant representing the actual plant and all weighting functions. K_1 represents the sensor dynamics including preamplifier gains, and K is the controller to be designed. Δ is the set of all possible uncertainties, grouped in to a single block-diagonal finite dimensional linear time invariant system. The diagram in Figure 2 is also referred to as a standard LFT formulation with lower linear fractional transformation (LLFT) on K, where P_gK_1 is the coefficient matrix of the LLFT and upper linear fractional transformation (ULFT) on Δ, where P_g is the coefficient matrix of the ULFT. LLFT is used in the controller design stage, and ULFT is used during the robust performance analysis stage.

The generalized plant, Figure 2 can be represented in frequency domain as follows:

$$\begin{bmatrix} z(z) \\ y(z) \end{bmatrix} = P_g(z) \begin{bmatrix} w(z) \\ u(z) \end{bmatrix} = \begin{bmatrix} P_{g_{11}}(z) & P_{g_{12}}(z) \\ P_{g_{21}}(z) & P_{g_{22}}(z) \end{bmatrix} \begin{bmatrix} w(z) \\ u(z) \end{bmatrix}, \tag{1a}$$

where the closed-loop transfer matrix from w to z can be given by

$$z = T_{zw} \cdot w, \tag{1b}$$

$$T_{zw} = P_{g11} + P_{g12}K_1 K\left(I - P_{g22}K_1K\right)^{-1}. \tag{1c}$$

The minimization of the H_2 norm of the transfer function from w to z, that is, T_{zw} over all realizable controllers $K(z)$, constitutes the H_2 control problem. The elements of the generalized plant P_g are obtained by augmenting the frequency-dependent weighting functions and corresponding output vector z into lower LFT form.

The present paper is concerned solely with the design, analysis, and validation of robust fixed-order H_2 controller by real-time hardware in the loop simulation for the lateral dynamics of Sarika-2. The controller design is based on the combination of strengthened discrete optimal projection equations (SDOPEs) [14], which are the modified version of the pioneering work of Bernstein et al. [15] on fixed-order controllers and frequency-shaped design techniques. In this paper, the time-domain weighting matrices of state and control variables [14] are changed to frequency-dependent weighting matrices. This enables the designer to shape the responses tighter in prespecified frequency ranges by giving them larger weights, clearly at the expense of larger errors at other frequency ranges that are of less importance. A good controller is the result of systematic tradeoffs between output sensitivity S_o, complementary sensitivity function T, and control sensitivity S_iK (S_i: input sensitivity function) of the closed-loop system. Since Sarika-2 is very small in size, the flow over the wing, where the velocity measuring pitot static probe is mounted, becomes turbulent at low Reynolds number flow regime. Also, light weight pressure sensors have poor sensitivity and stability in measurements. Further nonlinear relation between air speed and the dynamic pressure (total pressure-static pressure) makes such a device less preferred, since onboard correction for all above mentioned cants is not viable in Sarika 2 class of vehicles. Therefore, Sarika 2 does not have sensors to measure true or indicated air speed and hence, gain/controller scheduling over its flight speed range of 16–26 m/sec is not feasible. Therefore, a single discrete dynamic controller is designed at the central operating point (20 m/sec of flight speed) of the vehicle to achieve simultaneous stabilization, disturbance rejection, and sensor noise attenuation over the entire flight envelope of 16 m/sec–26 m/sec.

2. Lateral Dynamics of Sarika-2

Sarika-2 is a remote controlled small flying vehicle with a sweptback delta wing of 0.6 m span and planform area of 0.195 m^2. It has a square fuselage of width 0.06 m and a length of 0.8 m. It weights around 1.75 kg at take off. Control is achieved through independent actuation of outboard elevator, inboard aileron, and rudder. Sarika-2 has no horizontal tail. The power plant is a 4 cc propeller engine (OSMAX-LA 25), which uses methanol plus castor oil as fuel, with 10–15% nitromethane to boost the engine power.

Linearized state space models of lateral dynamics are developed in the stability axis [16], by assuming level flight at a constant altitude of 1000 m above the sea level (i.e., 100 m above the ground level at Bangalore) and trimming at six different operating speeds (i.e., at 16, 18, 20, 22, 24, and 26 m/sec). The state variables, $x \in R^4$ that describe lateral dynamics are sideslip angle β, roll rate p, yaw rate r, and bank angle ϕ. Static derivatives from the wind tunnel tests [1] are combined with the dynamic derivatives from the theoretical computation [17, 18] to provide complete set of stability derivatives [3] of the lateral dynamics of Sarika-2. Control surfaces are actuated by miniature electromechanical servo systems. Experimentally measured dynamics of the servo actuator (Futaba S3101 Micro Servo) is given by

$$\dot{\delta}_i = -9.5\delta_i - 6.37u_i, \tag{2}$$

where, $i = a$ and r for aileron and rudder respectively. δ_i is the aileron or rudder deflections in radians, and u_i is the width of the pulse width modulated (PWM) command input in milliseconds. The continuous state space model is discretized at 50 Hz (to synchronize with the command PWM input received at the vehicle from radio/pilot command from ground station). The final linearized model used for the controller synthesis includes two sampling period delay states to account for computational time requirements. Hence, the final model of the plant consists of eight states (four for MAV airframe, two for actuator and two for computational delay), two control inputs, wind disturbance input, and three sensor outputs from accelerometer and rate gyros. Discretized state space model of the lateral dynamics of Sarika-2, at the central operating condition of 20 m/sec is given by [3]

$$x_p(k+1) = A_p x_p(k) + B_{p1}u(k) + B_{p2}v_g(k), \tag{3a}$$

$$y(k) = C_p x_p(k) + D_{p1}u(k) + D_{p2}v_g(k), \tag{3b}$$

where v_g is the wind gust component in the lateral direction, $x_p = [\beta\ p\ r\ \phi\ \delta_a\ \delta_r]^T$, $u(k) = [\delta_{ac}\ \delta_{rc}]^T$, and $y = [a_y\ p\ r]^T$ measured with respect to the aircraft body axis (a_y is the lateral acceleration), and

$$A_p = \begin{bmatrix} 0.9778 & 0.0002 & -0.0194 & 0.0097 & -0.0036 & -0.047 & -0.0002 & -0.0028 \\ -1.8128 & 0.9664 & 0.0264 & -0.009 & -3.5364 & -0.0676 & -0.2578 & -0.006 \\ 1.0465 & -0.0041 & 0.9614 & 0.0052 & 0.1503 & 3.4276 & 0.0108 & 0.2501 \\ -0.0183 & 0.0197 & 0.0002 & 0.9999 & -0.0367 & -0.0009 & -0.002 & -0.0001 \\ 0 & 0 & 0 & 0 & 0.827 & 0 & 0.0955 & 0 \\ 0 & 0 & 0 & 0 & 0 & 0.827 & 0 & 0.0955 \\ 0 & 0 & 0 & 0 & 0 & 0 & 0.1353 & 0 \\ 0 & 0 & 0 & 0 & 0 & 0 & 0 & 0.1353 \end{bmatrix}, \tag{3c}$$

$$B_{p1} = \begin{bmatrix} 0.000 & 0.0001 \\ 0.0045 & 0.0001 \\ -0.0002 & -0.0044 \\ 0.0001 & 0.0000 \\ 0.0029 & 0 \\ 0 & 0.0029 \\ 0.1383 & 0 \\ 0 & 0.1383 \end{bmatrix}, \quad B_{p2} = \begin{bmatrix} 0.04889 \\ -0.0906 \\ 0.05233 \\ -0.00092 \\ 0 \\ 0 \\ 0 \\ 0 \end{bmatrix}, \tag{3d}$$

$$C_p = \begin{bmatrix} -11.797 & 0.0127 & -19.878 & 9.81 & -41.626 & -258.082 & 0 & 0 \\ 0 & 1.0000 & 0 & 0 & 0 & 0 & 0 & 0 \\ 0 & 0 & 1.0000 & 0 & 0 & 0 & 0 & 0 \end{bmatrix}, \tag{3e}$$

$$D_{p1} = \begin{bmatrix} 0 & 0 \\ 0 & 0 \\ 0 & 0 \end{bmatrix}, \quad D_{p2} = \begin{bmatrix} -0.5899 \\ 0 \\ 0 \end{bmatrix}. \tag{3f}$$

The stability augmentation system (SAS) is based on the feedback signals defined with respect to the stability axes. Hence, the measured variables are transformed from the body axes to stability axis using the following transformation:

$$\begin{bmatrix} p_s \\ a_{ys} \\ r_s \end{bmatrix} = \begin{bmatrix} \cos\alpha & 0 & \sin\alpha \\ 0 & 1 & 0 \\ -\sin\alpha & 0 & \cos\alpha \end{bmatrix} \begin{bmatrix} p_b \\ a_{yb} \\ r_b \end{bmatrix}, \tag{4}$$

where α is the trim angle of attack for a level flight at design speed of the nominal plant.

3. Design Specifications

The closed-loop design specifications for the lateral dynamics are determined from its expected responses [19] to pilot inputs sent from the aileron and rudder joystick. The main requirement of SAS is the improvement of handling qualities summarized as in Section 3.1.

3.1. Level 1 Flying Quality Requirements [19]

Dutch roll damping ratio ≥ 0.5.

Roll subsidence time constant < 1 sec.

Spiral mode: minimum time to double the amplitude > 12 sec.

Note from Table 1 that the specifications for the spiral and roll modes are satisfied at all flight speeds. However, the dutch-roll response is fast with poor damping, leading to large settling time. Consequently, the closed-loop specifications are to increase the dutch-roll damping to a minimum of 0.5.

3.2. Disturbance Rejection Specification. The standard turbulence parameters, L_v and σ_v [20] of the side wind gust, are modified to $L_v = 3$ m and $\sigma_v = 5.5$ m/sec^2 to take into account the worst case scenario, which occurs when all the dynamic modes of Sarika-2 are excited. The gust spectral density is evaluated as a function of cruise speed from 16 m/sec to 26 m/sec, and it is found that [3] the spectral bandwidth of gust increases with increase in speed (9.55 rad/sec at 26 m/sec). Hence, the disturbance rejection specification is as follows: minimize the sensitivity function below 0 dB for $\omega < 10$ rad/sec.

3.3. Sensor Noise Attenuation Specification. Experimentally, it is found that low cost sensors like rate gyros (Micro Gyro 100) and accelerometers (TAA-3804-100) have high-frequency noise content concentrated above 15 rad/sec. Therefore, to achieve high-frequency noise attenuation the specifications are as follows: obtain -40 dB/decade roll-off of the flight parameters above frequency of 15 rad/sec.

3.4. Robustness Specification. The controller designed at the central operating condition should be robust against the varying flight conditions in order to use a single controller at different operating points, which avoids gain/controller scheduling. The controller should also be robust against the structured real-valued parameter uncertainty within the context of state space models and unstructured multiplicative uncertainties on actuator inputs at all flight conditions. Larger uncertainty levels are placed on dynamic derivatives (50%), which are obtained analytically using DATCOM [17, 18], since the static derivatives (20%) obtained from the wind tunnel data are more reliable than those calculated using analytical approach.

Apart from the above specifications, closed-loop system should also be robust against the maximum expected time delays that may arise due to nonlinearity and computational complexity. In addition, the control surface deflections should not exceed its full-scale deflection of ± 16 degrees (± 0.4 milliseconds with respect to the neutral value of 1.5 ms of PWM input).

Table 1: Plant poles at different operating points.

Speed	Poles in w-domain	Damping	Frequency, Rad/sec	Mode
16 m/sec	$-0.138 \pm 5.92i$	0.0233	5.92	Dutch Roll
	-2.27	1	2.27	Roll Subsidence
	-0.436	1	0.436	Spiral
18 m/sec	$-0.27 \pm 6.63i$	0.0432	6.63	Dutch-roll
	-2.40	1	2.40	Roll Subsidence
	-0.415	1	0.415	Spiral
20 m/sec	$-0.394 \pm 7.35i$	0.056	7.36	Dutch-roll
	-2.55	1	2.55	Roll Subsidence
	-0.393		0.393	Spiral
22 m/sec	$-0.51 \pm 8.07i$	0.0657	8.08	Dutch-roll
	-2.71	1	2.71	Roll Subsidence
	-0.37	1	0.37	Spiral
24 m/sec	$-0.622 \pm 8.8i$	0.0731	8.81	Dutch-roll
	-2.88	1	-2.88	Roll Subsidence
	-0.348	1	0.348	Spiral
26 m/sec	$-0.728 \pm 9.53i$	0.0789	9.55	Dutch-roll
	-3.06	1	3.06	Roll Subsidence
	-0.328	1	0.328	Spiral

4. H_2 Optimal Control Formulation

Figure 3 represents the standard H_2 control formulation given in the form of general configuration known as linear fractional transformation (LFT), or two-port block diagram. Generalized plant P_g is obtained by augmenting the actual plant G_p with the weighting matrices. In Figure 3, $K_1 = \text{diag}([0.05 \;\; 1.2721 \;\; 1.2721])$ represents the sensor

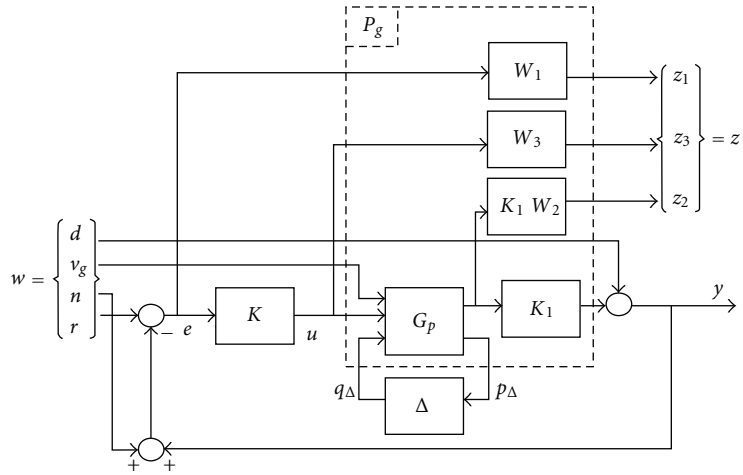

Figure 3: Standard H_2 control formulation.

sensitivity matrix including the preamplifier gains and K is the controller to be designed. The set of all possible uncertainties Δ is grouped in to a single block-diagonal finite dimensional linear time invariant system. The input signal vector w consists of all exogenous inputs comprising plant disturbances (d, v_g), sensor noise (n), and command input (r). The output of the controller is u, and y is a vector of measurement signals that are available for online control purpose. $W_1(z)$, $W_2(z)$, and $W_3(z)$ are frequency dependent weighting functions on S_o, T, and S_iK, respectively, whose outputs are represented in a vector form, $z = [z_1 z_2 z_3]^T$. Let T_{zw} denote the resulting closed-loop transfer function from w to z.

The objective of H_2 design is to find a fixed-order, discrete, optimal dynamic controller amongst all admissible controllers that yield internally stable closed-loop system so as to minimize the norm-2 of T_{zw}; that is,

$$\|T_{zw}(z)\|_2 = \left\| \begin{bmatrix} W_1(z)S_o(z) \\ W_2(z)T(z) \\ W_3(z)S_i(z)K(z) \end{bmatrix} \right\|_2, \tag{5}$$

where

$$S_o = (I + K_1GK)^{-1}; \qquad S_i = (I + KK_1G)^{-1},$$
$$T = \frac{K_1G(z)K(z)}{I + K_1G(z)K(z)}, \tag{6}$$

S_o is the transfer function between the external disturbance and the output and is a good measure of disturbance rejection, which is a low-frequency phenomenon. T, on the other hand, is a good measure of high-frequency noise attenuation, defined as the closed-loop transfer function between the input and output of the plant. Thus, W_1 is chosen as a low-pass filter and W_2 as a high-pass filter. Control-input constraint function is akin to putting penalty on actuator usage. The weighting function W_3 determines the robustness characteristics of the closed-loop system to unstructured additive uncertainties; that is, W_3^{-1} acts as the upper bound on the controller gains (S_iK). However, the crossover frequencies of S_o and S_iK or T (S_iK/T) are critical for both robustness and performance properties, since in the crossover frequency region of robustness and performance (S_o and S_iK/T) measures, neither S_o nor the T functions are small [21]. Choosing the performance weights to optimize the desired closed-loop performance, while maintaining the robust stability in the cross over frequency region is difficult [22].

Considering the state space representation of the plant and weights as,

$$G_p = \left[\begin{array}{c|cc} A_p & B_{p1} & B_{p2} \\ \hline C_p & D_{p1} & D_{p2} \end{array}\right], \qquad W_1 = \left[\begin{array}{c|c} A_{w1} & B_{w1} \\ \hline C_{w1} & D_{w1} \end{array}\right],$$
$$W_2 = \left[\begin{array}{c|c} A_{w2} & B_{w2} \\ \hline C_{w2} & D_{w2} \end{array}\right], \qquad W_3 = \left[\begin{array}{c|c} A_{w3} & B_{w3} \\ \hline C_{w3} & D_{w3} \end{array}\right], \tag{7}$$

and using the LFT theory [8], the closed-loop system with weighted cost functions are reformulated as

$$\begin{bmatrix} z(z) \\ y(z) \end{bmatrix} = P_g(z) \begin{bmatrix} w(z) \\ u(z) \end{bmatrix} = \begin{bmatrix} P_{g11}(z) & P_{g12}(z) \\ P_{g21}(z) & P_{g22}(z) \end{bmatrix} \begin{bmatrix} w(z) \\ u(z) \end{bmatrix}, \tag{8}$$

which yields the following state-space equations:

$$\begin{aligned} x(k+1) &= \Phi x(k) + B_1 w(k) + \Gamma u(k), \\ y(k) &= Cx(k) + D_1 w(k) + Du(k), \\ z(k) &= E_1 x(k) + E_3 w(k) + E_2 u(k), \end{aligned} \tag{9}$$

where $x(k) \in R^n$, $w(k) \in R^{m2}$, $z(k) \in R^{p2}$, $u(k) \in R^{m1}$, and $y(k) \in R^{p1}$, In addition, (Φ, Γ) is stabilizable, (Φ, C) is detectable, and the feed-forward matrix $E_3 = 0$ and E_2 and D_1 are full column and row rank matrix, respectively. Equation (9) can be rewritten in the expanded form as

$$\begin{bmatrix} x(k+1) \\ \hline z \\ \hline y \end{bmatrix} = \left[\begin{array}{ccc|ccccc|c} A_p & 0 & 0 & 0 & 0 & 0 & 0 & B_{p2} & B_{p1} \\ -B_{w1}K_1C_p & A_{w1} & 0 & 0 & B_{w1} & -B_{w1}K_1 & -B_{w1} & -B_{w1}K_1D_{p2} & -B_{w1}K_1D_{p1} \\ B_{w2}K_1C_p & 0 & A_{w2} & 0 & 0 & B_{w2}K_1 & 0 & -B_{w2}K_1D_{p2} & B_{w2}K_1D_{p1} \\ 0 & 0 & 0 & A_{w3} & 0 & 0 & 0 & 0 & B_{w3} \\ \hline -D_{w1}K_1C_p & C_{w1} & 0 & 0 & D_{w1} & -D_{w1}K_1 & -D_{w1} & -D_{w1}K_1D_{p2} & -D_{w1}K_1D_{p1} \\ D_{w2}K_1C_p & 0 & C_{w2} & 0 & 0 & D_{w2}K_1 & 0 & D_{w2}K_1D_{p2} & D_{w2}K_1D_{p1} \\ 0 & 0 & 0 & C_{w3} & 0 & 0 & 0 & 0 & D_{w3} \\ \hline -K_1C_p & 0 & 0 & 0 & I & -K_1 & I & -K_1D_{p2} & -K_1D_{p1} \end{array}\right] \begin{bmatrix} x \\ \hline r \\ d \\ n \\ \beta_g \\ \hline u \end{bmatrix}. \tag{10}$$

The goal of the fixed-order controller design is to find an n_cth order dynamic compensator $K(z)$ for the unknown A_c, B_c, C_c, and D_c

$$\begin{aligned} x_c(k+1) &= A_c x_c(k) + B_c y(k), \\ u(k) &= C_c x_c(k) + D_c y(k), \end{aligned} \tag{11}$$

so as to satisfy the following two design criteria.

(1) The closed-loop system corresponding to (10)-(11) given by

$$x_{\mathrm{CL}}(k+1) = A_{\mathrm{CL}} x_{\mathrm{CL}}(k) + D_{\mathrm{CL}} w(k), \qquad z(k) = E_{\mathrm{CL}} x_{\mathrm{CL}}, \tag{12}$$

where

$$\begin{aligned} x_{\mathrm{CL}} &= \begin{bmatrix} x \\ x_c \end{bmatrix}, \qquad A_{\mathrm{CL}} = \begin{bmatrix} \Phi + \Gamma D_c C & \Gamma C_c \\ B_c C & A_c \end{bmatrix}, \\ D_{\mathrm{CL}} &= \begin{bmatrix} \Gamma D_c D_1 \\ B_c D_1 \end{bmatrix}, \qquad E_{\mathrm{CL}} = \begin{bmatrix} E_1 & E_2 C_c \end{bmatrix} \end{aligned} \tag{13}$$

is asymptotically stable.

(2) The norm-2 of the closed-loop transfer function matrix

$$T_{zw} = E_{\mathrm{CL}}(zI - A_{\mathrm{CL}})^{-1} D_{\mathrm{CL}} \tag{14}$$

is minimized. Objective 2 leads to the steady state quadratic performance criterion

$$\begin{aligned} J(A_c, B_c, C_c, D_c) &= \lim_{N\to\infty} \frac{1}{N} \left\{ \sum_{k=1}^{N} T_{zw}{}^{*}\left(e^{j\omega k}\right) T_{zw}\left(e^{j\omega k}\right) \right\} \\ &= \lim_{N\to\infty} \frac{1}{N} \left\{ \sum_{k=1}^{N} s\left(x^{*}\left(e^{j\omega k}\right) Q\left(e^{j\omega k}\right) x\left(e^{j\omega k}\right) \right.\right. \\ &\qquad \left.\left. + u^{*}\left(e^{j\omega k}\right) R\left(e^{j\omega k}\right) u\left(e^{j\omega k}\right) \right) \right\}, \end{aligned} \tag{15}$$

$Q(z)$ and $R(z)$ (i.e., $Q(e^{j\omega k})$ and $R(e^{j\omega k})$) are obtained from the weighting matrices $W_1(z)$, $W_2(z)$, and $W_3(z)$ [3]. The controller parameters (A_c, B_c, C_c, and D_c) which minimizes the objective function J (15) are obtained by iteratively solving the following set of four coupled modified Riccati and Lyaponv equations known as SDOPEs [3, 14]:

$$\begin{aligned} P &= \Phi P \Phi^T - \textstyle\sum_P^1 + V + \tau_\perp \Psi^1_{S,\hat{P},P} \tau_\perp^T, \\ S &= \Phi^T S \Phi - \textstyle\sum_S^2 + Q + \tau_\perp^T \Psi^2_{P,\hat{S},S} \tau_\perp, \\ \hat{P} &= \frac{1}{2}\left[\tau \Psi^1_{S,\hat{P},P} + \Psi^1_{S,\hat{P},P} \tau^T \right], \\ \hat{S} &= \frac{1}{2}\left[\tau^T \Psi^2_{P,\hat{S},S} + \Psi^2_{P,\hat{S},S} \tau \right], \end{aligned} \tag{16}$$

provided P, S, $\hat{P}$, and $\hat{S}$ are nonnegative symmetric $n \times n$ matrices, $\mathrm{rank}(\hat{P}) = \mathrm{rank}(\hat{S}) = \mathrm{rank}(\hat{P}\hat{S}) = n_c$, and $\tau^2 = \tau = (\hat{P}\hat{S})(\hat{P}\hat{S})^{\#}$ (idempotent matrix) with

$$\begin{aligned} \sum_p^1 &= K_p W_p K_p^T, \qquad \textstyle\sum_s^2 = L_s^T R_s L_s, \\ \Phi_p^1 &= \Phi - K_p C, \qquad \Phi_s^2 = \Phi - \Gamma L_s, \\ \Psi^1_{S,\hat{P},P} &= \Phi_S^2 \hat{P} \left(\Phi_S^2\right)^T + \textstyle\sum_P^1, \\ \Psi^2_{P,\hat{S},S} &= \left(\Phi_P^1\right)^T \hat{S} \Phi_P^1 + \textstyle\sum_S^2, \qquad \tau_\perp = I_n - \tau, \\ W_p &= W + CPC^T, \qquad R_s = R + \Gamma^T S \Gamma, \\ K_p &= \Phi P C^T W_p^{-1}, \qquad L_s = R_s^{-1} \Gamma^T S \Phi. \end{aligned} \tag{17}$$

The optimality exists if the steady state cost functional J,

$$J(A_c, B_c, C_c, D_c)_\infty = J(A_c, B_c, C_c, D_c)_{Q,R} = J(A_c, B_c, C_c, D_c)_{V,W}, \tag{18}$$

where

$$\begin{aligned} J(A_c, B_c, C_c, D_c)_{Q,R} &= \mathrm{tr}\left[QP + \left(Q + L_S^T R_S L_S \right) \hat{P} \right], \\ J(A_c, B_c, C_c, D_c)_{V,W} &= \mathrm{tr}\left[VS + \left(V + K_P W_P K_P^T \right) \hat{S} \right]. \end{aligned} \tag{19}$$

The controller then can be computed as:

$$\begin{aligned} A_c &= H\left[\Phi - K_p C - \Gamma L_s \right] G^T; \qquad B_c = H K_p, \\ C_c &= L_s G^T; \qquad D_c = 0, \end{aligned} \tag{20}$$

for some projective factorization (G, M, H) of $(\hat{P}\hat{S})$.

5. Results and Discussions

The controller is designed at the central operating point of Sarika-2 (i.e., at 20 m/sec) and is used for all flight conditions. The weighting matrices W_1 and W_2 need to be strictly proper in order to make the feed through term, E_3 zero. Following the guidelines [23] to select the weighting matrices, the final choice of the weighting matrices, W_1, W_2 and W_3 (in discrete domain) are

$$W_1(z) = \begin{bmatrix} \frac{0.89(z-0.99)}{(z-0.25)(z-0.67)} & 0 & 0 \\ 0 & \frac{1.19(z-0.99)}{(z-0.45)(z-0.74)} & 0 \\ 0 & 0 & \frac{0.02(z-0.99)}{(z-0.82)(z-0.99)} \end{bmatrix},$$

$$W_2(z) = \begin{bmatrix} \frac{0.38(z-0.99)}{(z-0.14)^2} & 0 & 0 \\ 0 & \frac{(z-0.82)}{(z-0.37)^2} & 0 \\ 0 & 0 & \frac{4.12(z-0.82)}{(z-0.14)^2} \end{bmatrix}, \tag{21}$$

$$W_3(z) = \begin{bmatrix} \frac{1.6(z-0.98)}{(z-0.25)} & 0 \\ 0 & \frac{2.2(z-0.98)}{(z-0.25)} \end{bmatrix}.$$

The weighting matrix W_1 minimizes the sensitivity function, which is a low-frequency signal. Hence, the cutoff frequency of W_1, a low-pass filter, is selected to minimize the sensitivity within the range of the operating frequency of Sarika-2 (10 rad/sec). Weighting matrix W_2 is chosen to reduce the effect of measurement noise, which results due to the reduction of cosensitivity outside the range of the operating frequency of the vehicle (above 10 rad/sec). W_3 helps in minimizing the control effort at high-frequency region. So, it must be a high-pass filter, with a cutoff frequency of 10 rad/sec.

With the choice of the weighting matrices as indicated in (21), the order (n) of the generalized plant is 24 (4 states for MAV airframe, 2 states for actuator, 2 states for delay units, and 16 states for weighting matrices W_1, W_2, and W_3). Since the design of fixed low-order controller does not address optimal/minimal order of the controller that can meet design specifications, controllers of order 1 to 5 are designed separately and stability and performance characteristics of controllers of decreasing order are compared with the full (24th) order controller. The first column of Table 2 gives the order of controllers designed separately. Columns 2 and 3 contain the values of cost functions, $J(A_c, B_c, C_c, D_c)_{Q,R}$ and $J(A_c, B_c, C_c, D_c)_{V,W}$ computed using (19). The first-order necessary optimality conditions are satisfied in each case, which is illustrated by the fact that $J(A_c, B_c, C_c, D_c)_{Q,R}$ and $J(A_c, B_c, C_c, D_c)_{V,W}$ are nearly equal [14].

The cost function is almost constant (around $J = 2455$) for $n_c = 24$ and 5 to 3, which implies that by increasing the order of the controller above 3, this does not significantly improve the performance of the closed-loop system. Similarly, increase in the cost function from $J = 2455$ to $J = 2498$ by reducing the order of the controller from $n_c = 3$ to $n_c = 2$ implies the performance deterioration of the closed-loop system. Hence, the minimal order of the controller is 3. Fourth column of Table 2 indicates that the robustness against the additive uncertainty $(S_iK)_{,}^{-1}$ remains at 1.497 and does not show any improvement by increasing the order of the controller above 3. Also, with third-order controller, the quadratic stability (Column 5 of Table 2) is assured around 125.01% of the parametric uncertainty levels in contrast to that of only 93.3%, which is obtained with second order controller. This implies that with third-order controller, the closed-loop system is capable of withstanding at least 125.0133% of the assumed plant uncertainty, without being destabilized. There exists a parameter-dependent Lyapunov function in each case, which is indicated by a negative t (for feasibility) in column 6 of Table 2. Existence of parameter-dependent Lyapunov function implies robust stability against the slowly varying uncertainties [24, 25].

Figure 4 shows the comparison of the frequency responses of third- and 24th-order controllers. The frequency response remains in close neighborhood for two controllers in the frequency range of 1 to 100 rad/sec. This further substantiates the selection of third-order controller.

The six elements of transfer function matrix of the third order controller $K_{2\times 3}$ are given by

$$K(z) = \frac{1}{\Delta(z)} \begin{bmatrix} -0.48(z-0.85)(z-0.98) & -0.58(z-0.85)(z-0.99) & 0.21(z-0.86)(z-0.98) \\ -0.09(z-0.57)(z-0.98) & -0.11(z-0.575)(z-0.99) & 0.04(z-0.57)(z-0.98) \end{bmatrix}, \tag{22}$$

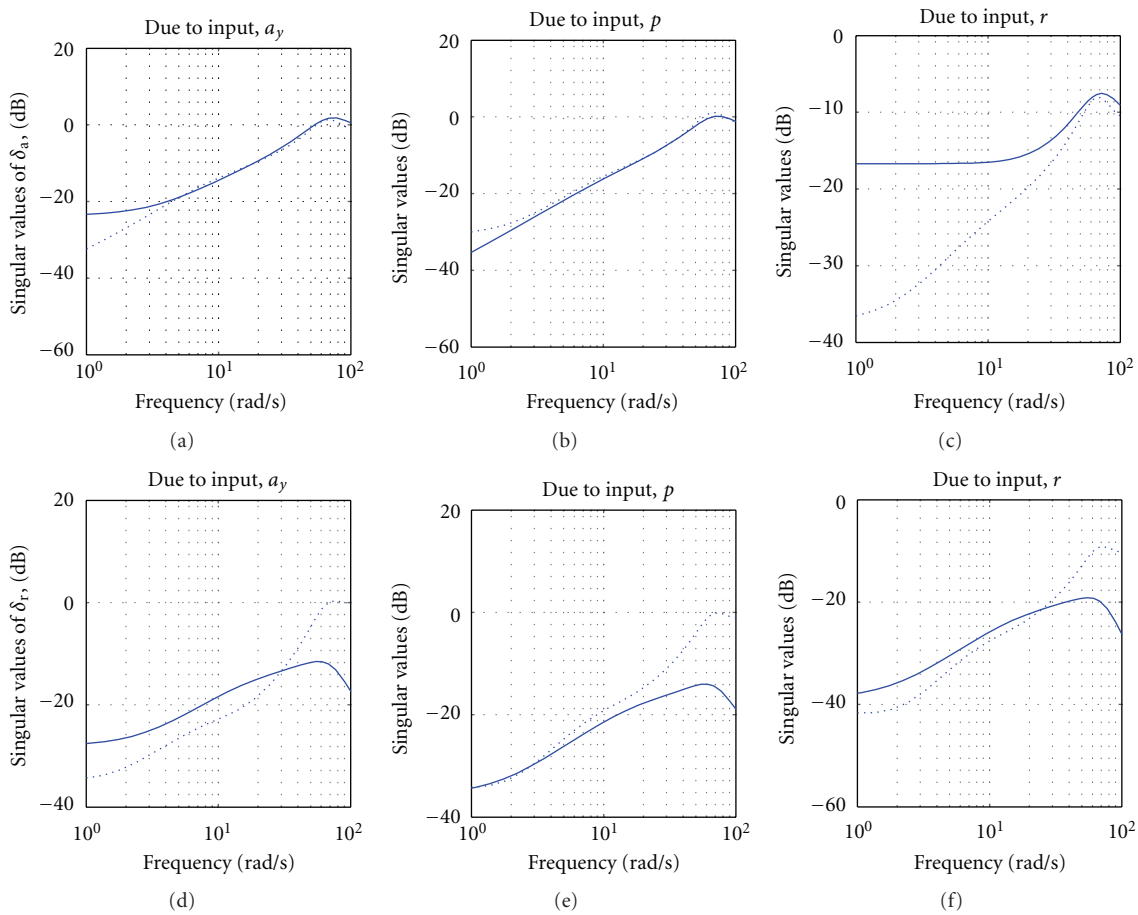

Figure 4: Frequency response of 3rd (—) and 24th (·····) order controllers.

Table 2: Simulation results.

n_c	$J(A_c, B_c, C_c, D_c)_{Q,R}$	$J(A_c, B_c, C_c, D_c)_{V,W}$	$(S_iK)^{-1}$	Test for Quadratic stability	Test for Robust stability, t	μ-upper bound
24	2455.04	2455.01	1.2	113.2%	-1.12×10^{-4}	1.45
5	2455.05	2455.02	1.208	114.14%	-1.13×10^{-4}	1.467
4	2455.54	2455.47	1.25	138.89%	-7.27×10^{-3}	1.958
3	2455.67	2455.51	1.497	125.01%	-6.5×10^{-6}	1.802
2	2498.64	2506.26	0.629	93.323%	-0.010193	1.371
1	3397.22	3397.26	0.159	Unstable	Unstable	Unstable

where $\Delta(z) = (z - 0.945)(z^2 - 0.6687z + 0.1265)$. The frequency responses of the transfer function from lateral acceleration a_y, roll rate p, and yaw rate r to aileron and rudder input channels show wash out or lead filter characteristics. This implies that the control surfaces are active only during the transient and are unaffected when the outputs reach steady state, which is desirable. The phase lead of the controller helps in overcoming the phase lag of the low bandwidth and light weight actuator. The closed-loop dutch-roll damping is calculated at different flight conditions (using the controller designed at the flight speed of 20 m/sec). As per the design specifications, the dutch-roll damping remains above 0.5 at all the flight conditions.

6. Performance and Robustness Analysis

Plots of the singular values of S_o, S_iK and T (6) with a third-order controller at three different flight speeds (16 m/sec, 20 m/sec and 26 m/sec) are shown in Figure 5.

Singular values of S_o for the lateral acceleration, roll rate, and yaw rate loops show slight deviation from one another at low frequencies (below 8 rad/sec), having a magnitude in the neighborhood of 0 dB in the negative side. Larger attenuation of the singular values of the yaw rate compared to that of the lateral acceleration and roll rate indicates that among the three outputs, yaw rate and hence beta response is least affected by the output disturbances. The nonminimum phase

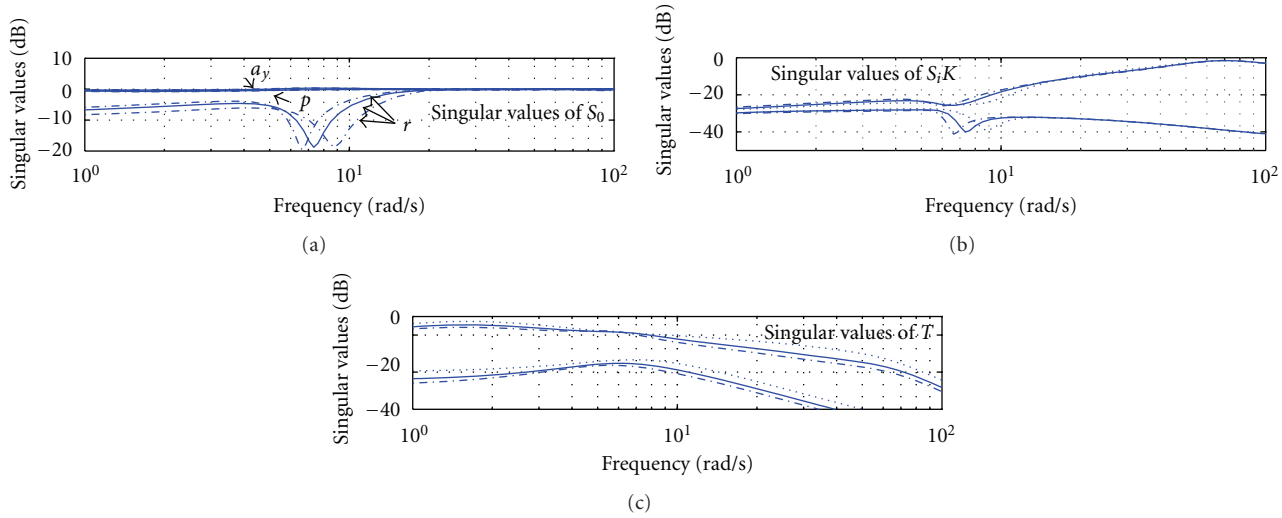

Figure 5: Singular values of S_o, S_iK and T (16 m/s: dotted line, 20 m/s: bold line, 26 m/s: dash-dot line).

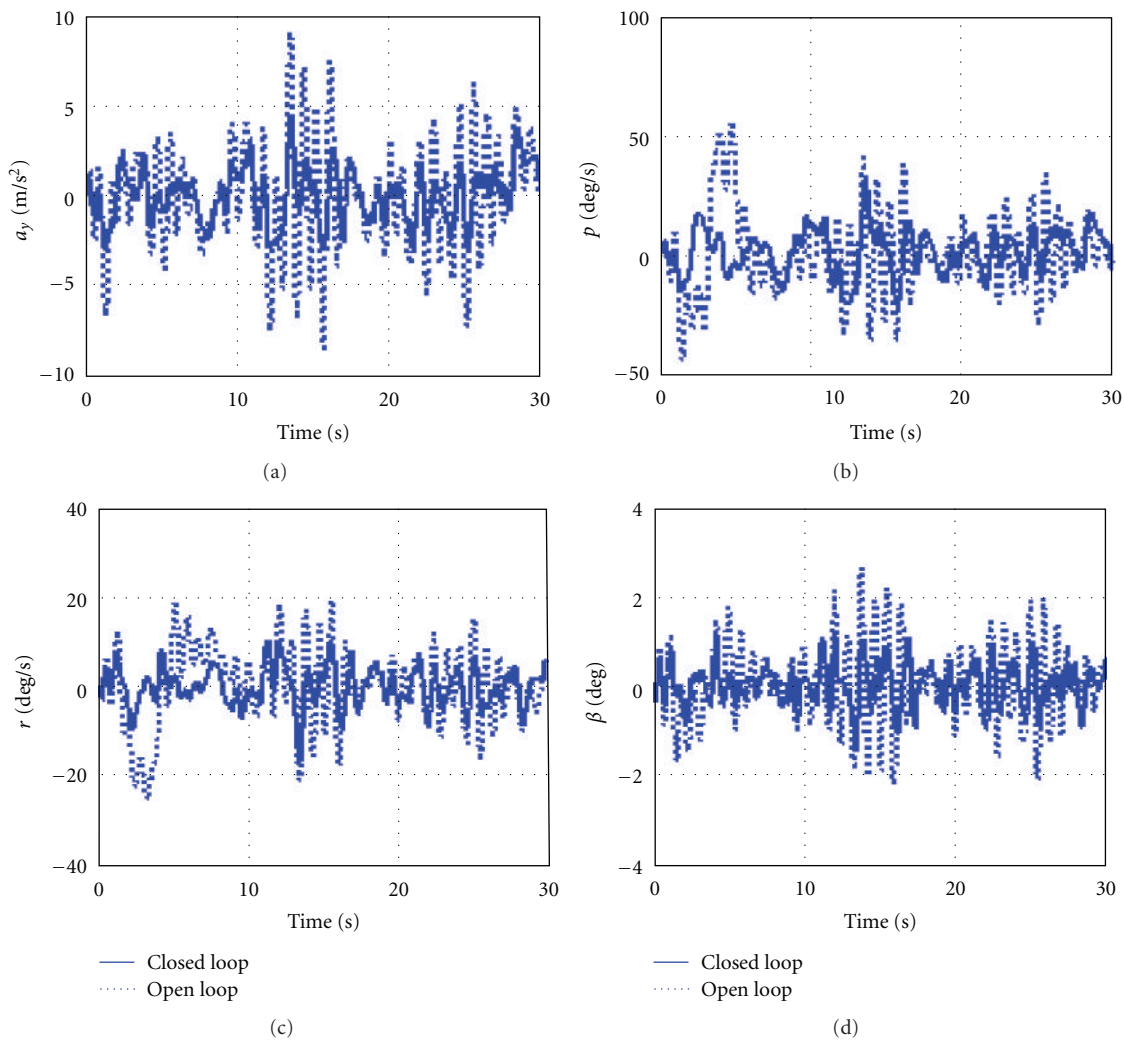

Figure 6: Response to gust input.

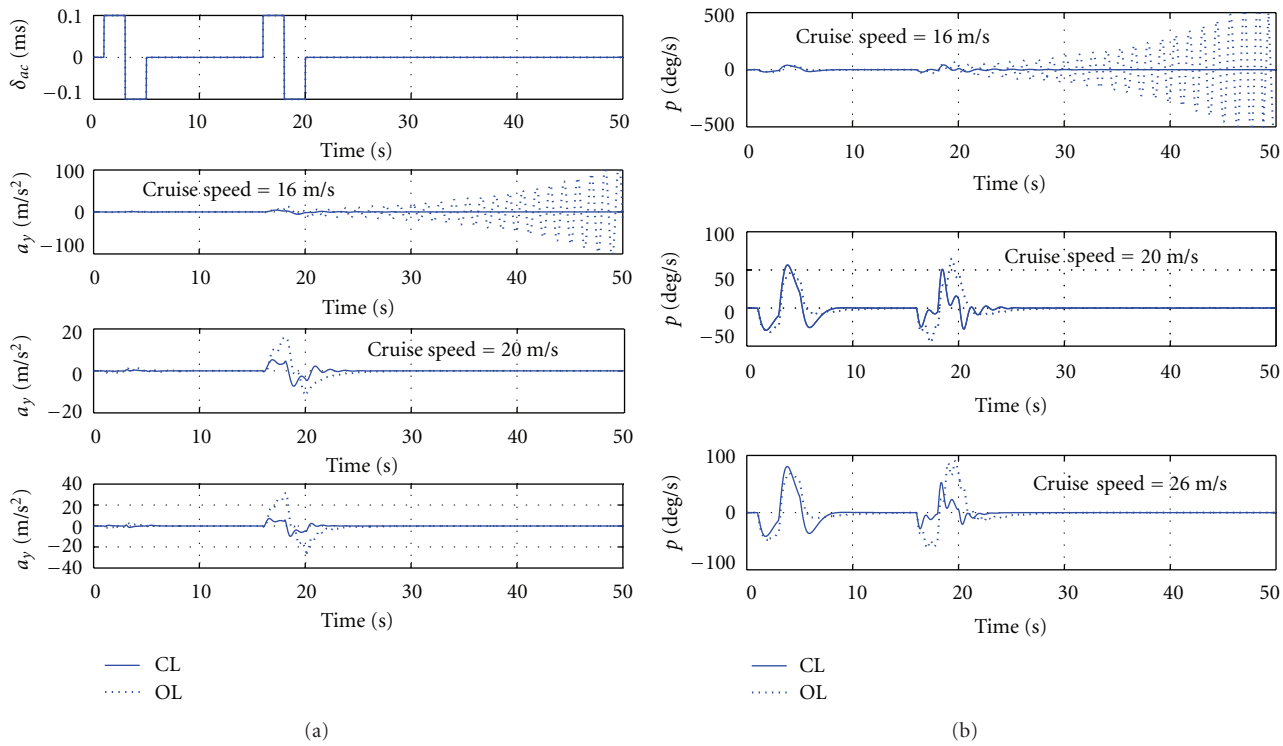

Figure 7: Responses of a_y and p of the nominal and perturbed plant (solid line: closed-loop response, dotted line: plant response).

zeros of the open-loop system limits the lower bound of the sensitivity that can be achieved. Low values of S_iK at low frequencies (up to 40 rad/sec) indicate very good stability robustness properties of the closed-loop system against the additive uncertainty, Δ_a. Though the upper bound of S_iK increases in the frequency range beyond 40 rad/sec, it is well within the 0 dB, indicating positive gain margin. This property is preserved at all flight conditions. The singular values of T show an attenuation of -60 dB/decade beyond $\omega = 10$ rad/sec, corroborating good noise attenuation by a factor of 1000, which is acceptable.

Figure 6 gives responses of the closed-loop system and plant (aircraft) due to atmospheric turbulence.

Turbulence input is generated by passing a zero mean and variance of 0.01 m^2/s, band limited white noise through a forming filter [3, 20]. Closed-loop responses (— lines) of a_y, p, r, and β in Figure 6 show a significant reduction in magnitude compared to the corresponding plant responses (····· lines) (attenuation of 50% on a_y response, 33% on β response). In other words, the variance of a_y of the closed-loop system is reduced to 2.2558 m/sec^2 from 8.6635 m/sec^2. Similarly, the variances of p, r, and β of the closed-loop system reduce to 90.0325 deg/sec, 27.5604 deg/sec, and 0.3089 degrees from their corresponding values of plant response of 316.9422 deg/sec, 111.4768 deg/sec, and 1.0575 degrees respectively.

6.1. Perturbation Analysis. The robust stability and performance of the closed-loop system at all flight conditions (using a controller designed at the nominal flight speed of 20 m/sec) are further demonstrated by using LMI-based tests [24, 25]. For this, affine parameter-dependent plant models are developed by assuming structured real-valued parametric uncertainties (i.e., by perturbing the stability derivatives of the vehicle) at each of the flight conditions. At 20 m/sec of cruise speed, the quadratic stability of the closed-loop system is established with 125.0133% of the prescribed uncertain parameter box. Likewise, at 16 m/sec and 26 m/sec of cruise speeds, the quadratic stability of the closed-loop system is preserved with 103.185% and 101.861% of the uncertain parameter box, respectively. For the same uncertainty levels, μ upper bound is around 0.5549, 0.6454, and 0.6745 at cruise speeds of 20, 16 and 26 m/sec, respectively. Thus, largest amount of uncertainty Δ that can be tolerated without losing stability is 1.802, 1.549, and 1.483, which is greater than the required lower bound of 1.0.

6.2. Time Response Study. Roll rate command is applied to aileron control stick in the form of pulse width modulated signal given in the units of milliseconds (with respect to the neutral or bias value of 1.5 msec, which corresponds to the zero deflection of the aileron control surface). In the simulation study, a 20 msec delay is included at the input of the aileron and rudder, which accounts for the computational delays. A wideband sensor noise of zero-mean and variance of 0.005 volts is introduced in the simulation. At first, the aircraft is trimmed for straight and level flight at an altitude of 1000 m above the sea level (i.e., 100 m above the ground level at Bangalore). A positive pulse of two-second duration and an amplitude of 0.1 msec (with respect to the

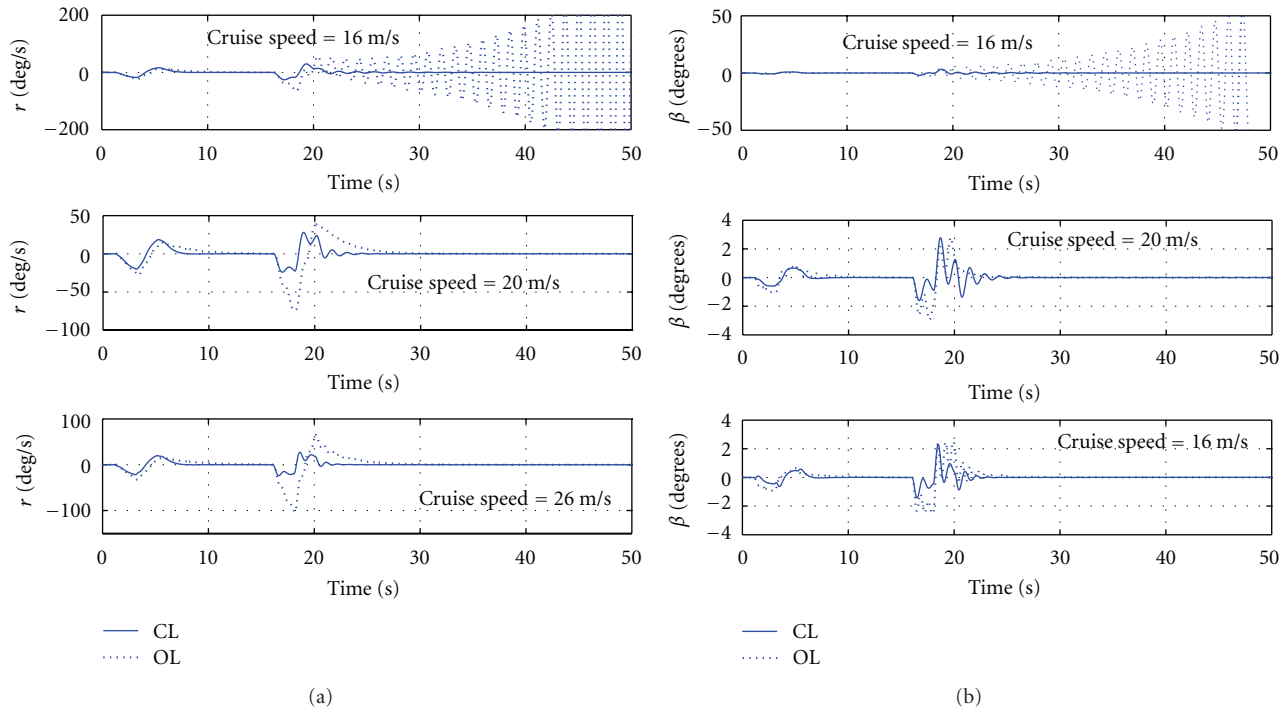

Figure 8: Responses of r and β of the nominal and perturbed plant (solid line: closed-loop response, dotted line: plant response).

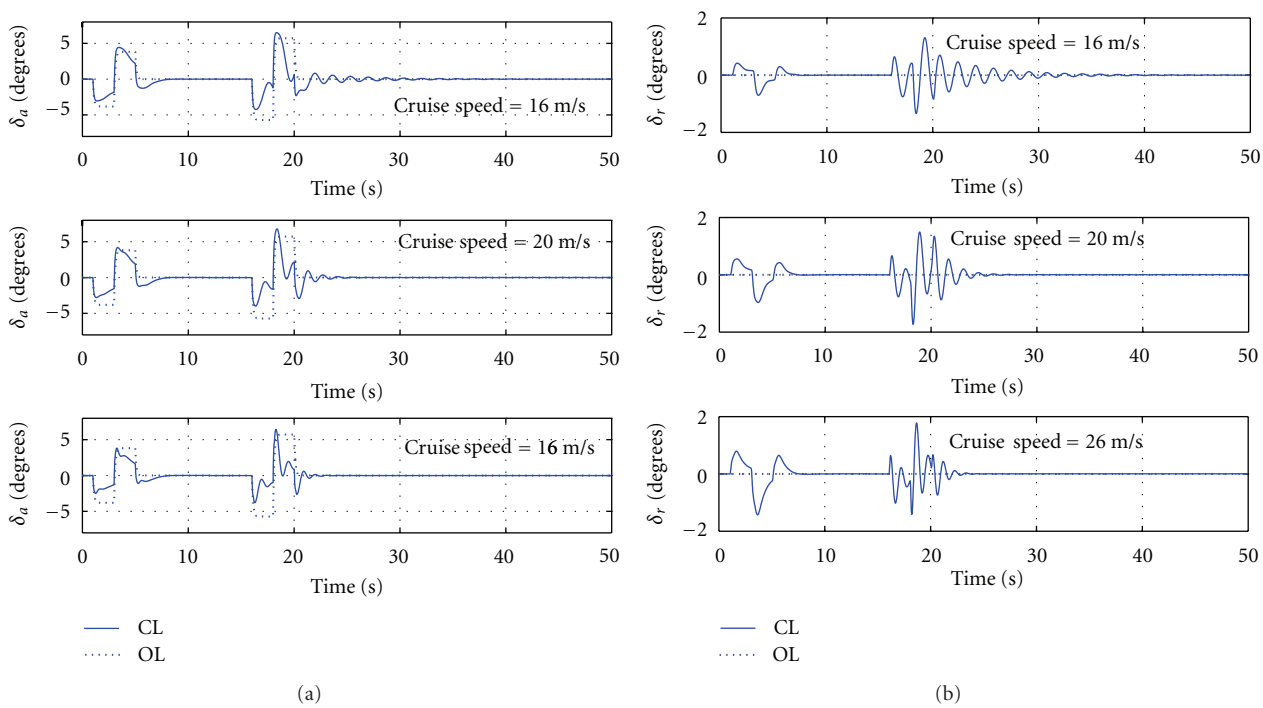

Figure 9: Responses of δ_a and δ_r of the nominal and perturbed plant (solid line: closed-loop response, dotted line: plant response).

nominal value of 1.5 msec) corresponding to -3.84 degree aileron deflection is applied to the aileron channel at $t = 1$ sec. This input is followed by a negative pulse of two second duration and amplitude of 0.1 msec, which corresponds to a 3.84 degree aileron deflection. This input pattern is equivalent of moving the aileron channel joystick from its neutral point to one side then to the other side and back to the neutral point. Simulation study is presented for the three models corresponding to the cruise speeds of 16, 20, and 26 m/sec.

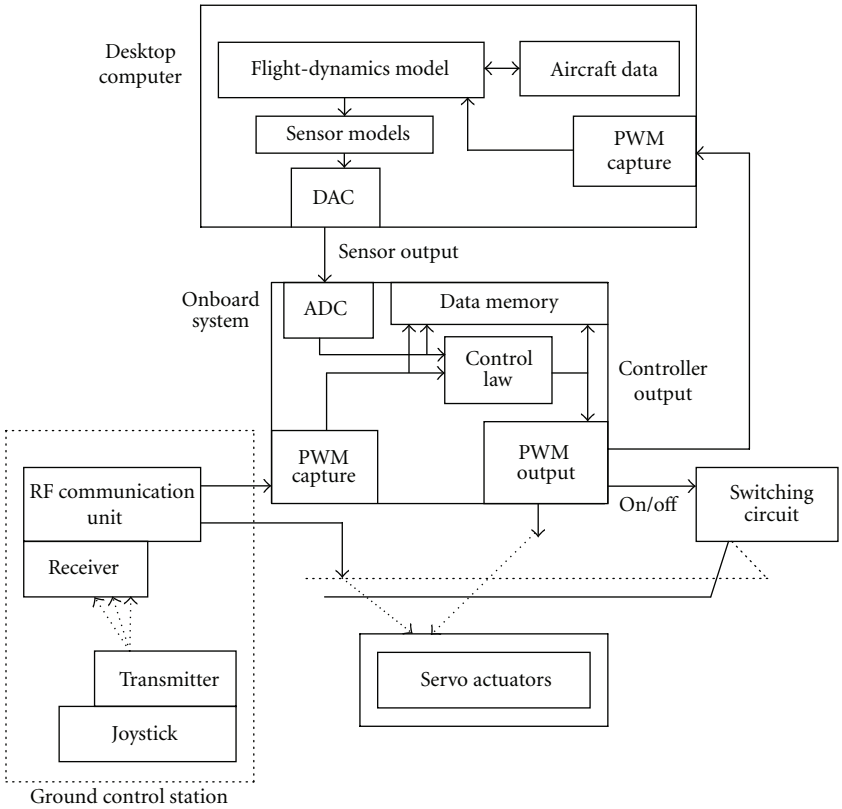

Figure 10: Block diagram representation of HILS.

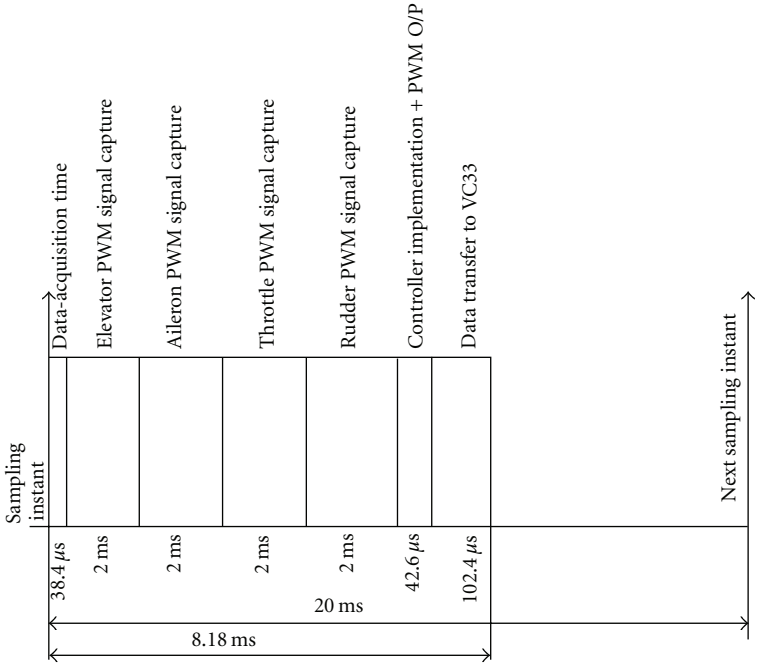

Figure 11: Task scheduling for the control law implementation.

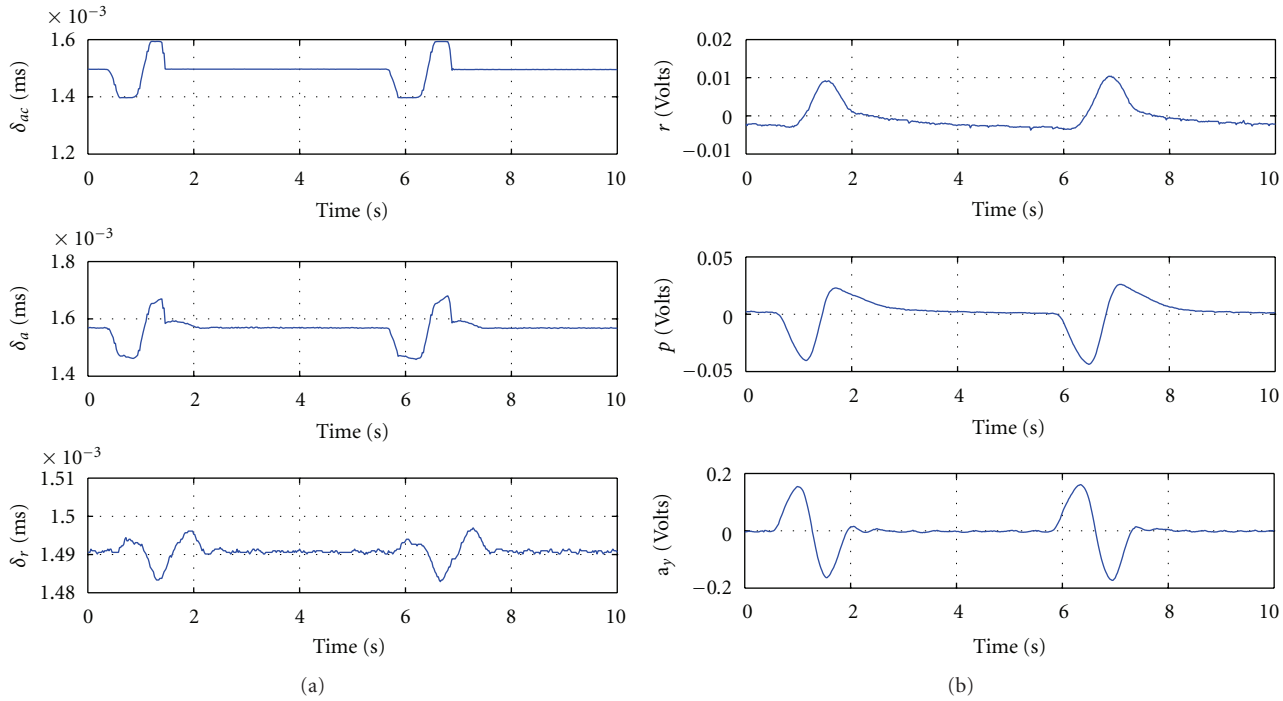

Figure 12: Command input, controller output and HILS responses of a_y, p, and r.

Figures 7, 8, and 9 give the time responses of the closed-loop system to the above-mentioned command input. For the better appreciation of the performance robustness of the closed-loop system, the time responses are also simulated by perturbing the plant matrices (by 50% and 20% on dynamic and static stability derivatives, resp.). In Figures 7–9, the response plots up to 15 sec correspond to the unperturbed (nominal) plant whereas plots for time $t > 15$ sec correspond to the perturbed plant. Though the responses of the perturbed plant are highly oscillatory, the closed-loop system responses of both perturbed and nominal plants settle down relatively faster than that of uncontrolled aircraft responses. Clearly, the fixed gain controller robustly stabilizes all the nominal and perturbed plants at the three cruise speeds, whereas the perturbed plant response (at 16 m/sec of flight speed) diverges leading to instability. The instability of the perturbed plant is due to the shift of the aerodynamic centre ahead of the centre of gravity of the aircraft. In addition, gust disturbance and sensor noise are rejected at all flight conditions. The closed-loop system responses of both a_y and β for nominal and perturbed plant are appreciably attenuated. Further, the closed-loop responses of p and r are well damped with a fast settling time of 7 sec. The fast settling and well-damped responses for both nominal and perturbed plant models at all flight conditions, with the fixed gain controller, demonstrate the robust performance against the parameter variation. Control surface deflections in Figure 9 show that deflections are well within its upper bounds of ± 16 degrees when the PWM command signal reaches its maximum value of ± 0.4 msec. For the given positive aileron deflection, note that the rudder deflections are negative by virtue of which rudder coordinates the turn avoiding adverse yaw effects.

7. Real-Time Hardware-in-the-Loop-Validation of the Controller

Experimental setup of hardware-in-loop-simulation (HILS) includes a simulation computer and onboard computer named flight instrumentation computer (FIC) built with two digital signal processors (DSPs): TMS320LF2407 and TMS320VC33 from Texas Instruments, USA. Onboard computer hardware (of size 139.7 mm × 50.8 mm and weight 55 grams) has been developed in-house. The integration of an on board computer, capable of real-time implementation of flight control, within Sarika-2 is a technically challenging task owing to the stringent constraints on cost, size, weight, and power limitations. The FIC has additional onboard program (256 Kbytes) and data (4 Mbytes) memories. FIC is capable of acquiring data (with 10 Hz low-pass filter and necessary signal conditioning with a gain of 20 on rate channel and a unity gain on acceleration channel), internal data logging, executing multi-input multi-output discrete control logic in real time, and generation and capturing of PWM signals.

The simulation computer is Pentium 4 PC (Windows 2000 OS) operating at 3.4 GHz with dSPACE DS1104RTI/RTW. The DS1104 is a complete real-time control system which is based on a Power PC 603 floating-point processor running at 250 MHz. The constitutive building blocks of the HILS facility or setup are given in Figure 10. The lateral flight dynamic model, running on the desktop computer, calculates

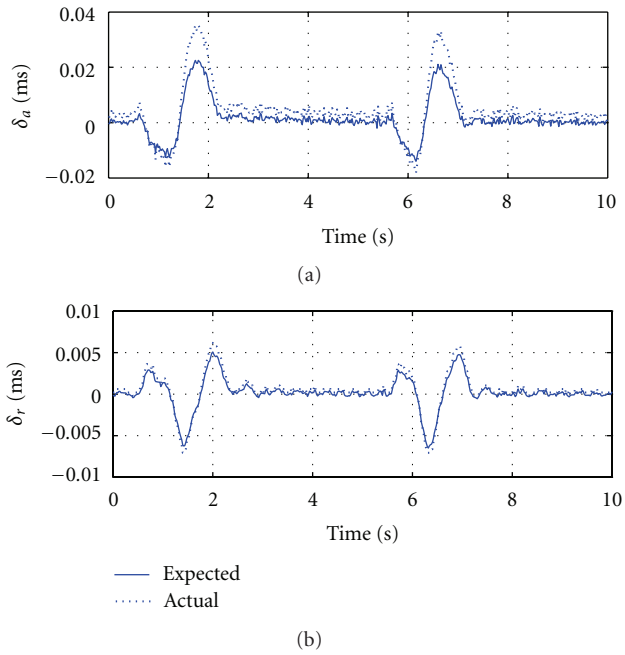

Figure 13: Comparison between the actual and expected output of the controller.

the vehicle's roll rate, yaw rate, and lateral acceleration response, and DS1104 system subsequently generates the equivalent analog sensor signal in volts. Sensitivities of MEMS-based sensors used for Sarika-2 are (1) rate gyros: 1.11 mv/deg/s (with an offset voltage of 2.25 volts) and (2) Accelerometer: 500 mv/g (with a bias of 2.5 volts). Hence, the electrical output of sensors are simulated (sent out through digital to analog converter, DAC of DS1104), according to the relation,

$$V_{\text{eq}}(p \text{ or } r) = 0.063603 \times (p \text{ or } r) + V_{\text{offset}}(p \text{ or } r),$$
$$V_{\text{eq}}\left(a_y\right) = 0.05 \times \left(a_y\right) + V_{\text{offset}}\left(a_y\right). \tag{23}$$

7.1. Controller Implementation and Validation. The control law realization on FIC comprises four main routines that is: (1) initialization routines (2) delay routine to erase the flash memory in order to store new set of flight data (3) sensor Calibration routines, and (4) interrupt routines. Owing to the requirement of updating the servos for every 20 msec, entire task scheduling (Figure 11) is repeated for every 20 msec.

In order to meet the critical requirement of updating servo position for every 20 msec, a software timer period interrupt, which sequences the four functions (data acquisition, PWM capture, control law calculation, and PWM generation), is enabled. Software capture interrupt is enabled so as to receive the latest pilot command inputs from the radio-controlled transmitter. An external hardware interrupt XINT2, which has the highest priority, is also enabled that can momentarily halt the control law calculation and data acquisition. XINT2 interrupt is used to retrieve the flight data from the flash memory to the personal computer. As shown in Figure 11, processor completes the entire task in 8.18 msec and waits for the period interrupt to start the next cycle. Hence, there will not be any timing mismatch or clash between the PWM signals sent from the transmitter and from the controller.

The control law coded on FIC is validated using HILS experimental setup, which provides a real flight environment to the controller. FIC receives the real-time hardware in the loop simulated sensor signals (given in (23)) from DAC unit of dSPACE1104 RTI/RTW and PWM signals (which is transmitted from joystick controller by the ground pilot) from the RF receiver, Futaba R136F. Since the inputs to the controller are in volts (from the sensors) and the outputs needs to be in milliseconds to drive the actuators, a relation (or conversion factor) between the voltage to PWM signal width is found experimentally as

$$\text{PWM signal width} = \left(V_{\text{signal}} - V_{\text{offset}}\right) \times 1.18\,\text{msec}. \tag{24}$$

The FIC continuously receives the analog signals from dSPACE 1104 and converts it into an equivalent PWM signals. On the basis of these two inputs, controller outputs are generated and are feedback to the simulated actuators through the capture unit of dSPACE1104 RTI/RTW.

The real-time command signals received by the radio frequency receiver and the emulated sensor signals from the HILS (corresponding to the flight speed of 20 m/sec) are plotted in Figure 12. The aileron input is a doublet of −0.1 to 0.1 ms (with respect to the neutral value of 1.5 msec, i.e., ±3.84 degree aileron deflection). The rudder command is held at its neutral position. The aircraft response shows a roll rate varying from −0.04 volts (≈−36 degrees/sec) to 0.02 volts (≈18 degrees/sec). Therefore, the aileron input of −0.4 msec, with respect to the neutral position, corresponds to a maximum roll rate of −144 deg/sec, while a 0.4 msec aileron input corresponds to a maximum of 72 degrees/sec. Similarly, yaw rate response varies between a maximum of 0.01 volts (≈9 degrees/sec) to −0.004 volts (≈−4 degrees/sec). The lateral acceleration varies between ±0.16 volts (≈±0.3 g), implying a maximum of 1.2 g excursion when the input is ±0.4 ms with respect to the neutral position.

Comparison between the actual and expected output of the controller at 20 m/sec of cruise speed is shown in Figure 13. The actual outputs are obtained from the FIC, and the expected outputs are obtained from the simulation using SIMULINK tools. A delay of 0.1 sec is noticed between the actual and expected output of the controller, which is due to the transportation delay unit introduced during simulation (in dSPACE 1104). However, this delay will not occur in reality. On the aileron channel, the actual output shows a small offset of ±0.01 msec with respect to that of simulated output. On the other hand, the mismatch on rudder channel is almost zero. In real applications, a 0.01 msec of offset in PWM signal on the aileron channel gives a disparity of 0.4 degree of aileron deflection. However, since the controller is robust, this mismatch is acceptable.

8. Conclusions

Design and development of a discrete fixed-order robust H_2 flight stabilization system for microair vehicle, named Sarika-2, is presented. This paper illustrates the design of a robust fixed-order H_2—optimal controller using frequency-dependent weighting functions, on the basis of strengthened discrete optimal projection equations. The reduced fixed-order H_2 controller, designed by a direct single-step procedure, ensures both stability and optimality of the closed-loop system. The controller also imparts robust performance against 50% and 20% parametric uncertainties of the dynamic and static stability derivatives. The perturbation analysis also demonstrates that it is possible to stabilize an unstable perturbed plant by a controller designed for a single plant. The washout characteristic of feedback loops makes control activity zero during steady state operation. The controller allows the wing to autolevel immediately after execution of coordinated turn or withdrawal of side wind gust input, which is beneficial for reconnaissance missions. Time responses of the closed-loop simulation, using real-time hardware in the loop simulation experimental setup, match well with the responses of corresponding offline simulation. Thus, the robust fixed-order H_2 controller implemented on flight instrumentation computer can be successfully used for the flight control of Sarika-2 microair vehicle.

References

[1] B. R. Srinivasa Rao, V. Surendranath, and H. R. S. Prasanna, "Wind tunnel test results of SARIKA airplane," Tech. Rep. AE/WT/IRR/16, Department of Aerospace Engineering, Indian Institute of Science, Bangalore, India, 2001.

[2] B. M. Seetharama, M. Meenakshi, S. P. Govindaraju et al., "Design and development of flight control and instrumentation for micro air vehicle," Tech. Rep. ARDB/MSB/TR-99-1050, Department of Aerospace Engineering, Indian Institute of Science, Bangalore, India, 2002.

[3] M. Meenakshi, *Design and real time validation of discrete, fixed order, robust, H_2 controller for micro air vehicle*, Ph.D. thesis, Indian Institute of Science, Bangalore, India, 2005.

[4] W. Gawronski, JPL, C. A. Pasadena et al., "Frequency weighting for the H-infinity and H_2 control design of flexible structures," *Journal of Guidance, Control, and Dynamics*, vol. 21, no. 4, pp. 664–666, 1998.

[5] L. C. Marco, P. George, C. M. William, and K. Takeo, "Design and flight testing of a high-bandwidth H_∞ loop shaping controller for a robotic helicopter," Tech. Rep. 4836, AIAA, 2002.

[6] A. A. Stoorvogel, "The singular H_∞ control problem with dynamic measurement feedback," *SIAM Journal on Control and Optimization*, vol. 29, no. 1, pp. 160–184, 1991.

[7] R. A. Hyde and K. Glover, "The application of scheduled H_∞ controllers to a VSTOL aircraft," *IEEE Transactions on Automatic Control*, vol. 38, no. 7, pp. 1021–1039, 1993.

[8] M. Green and D. J. N. Limebeer, *Linear Robust Control, Prentice Hall*, Englewood Cliffs, NJ, USA, 1995.

[9] K.-C. Goh and F. Wu, "Duality and basis functions for Robust H_2-performance analysis," *Automatica*, vol. 33, no. 11, pp. 1949–1959, 1997.

[10] D. Banjerdpongchai and J. P. How, "Parametric robust H_2 control design using iterative linear matrix inequalities synthesis," *Journal of Guidance, Control, and Dynamics*, vol. 23, no. 1, pp. 138–142, 2000.

[11] D. G. Bates and I. Postlethwaite, "The structured singular value and μ- analysis," in *Advanced Techniques for Clearance of Flight Control Laws*, C. Fielding, A. Varga, S. Bennani, and M. Selier, Eds., chapter 3, pp. 37–55, Springer, Heidelberg, Germany, 2002.

[12] N. Kannan and M. Seetharama Bhat, "Longitudinal H_∞ stability augmentation system for a thrust-vectored unmanned aircraft," *Journal of Guidance, Control, and Dynamics*, vol. 28, no. 6, pp. 1240–1250, 2005.

[13] Y. Liu and B. D. O. Anderson, "Controller reduction: concepts and approaches," *IEEE Transactions on Automatic Control*, vol. 34, no. 8, pp. 802–812, 1989.

[14] L. G. van Willigenburg and W. L. de Koning, "Numerical algorithms and issues concerning the discrete-time optimal projection equations," *European Journal of Control*, vol. 6, no. 1, pp. 93–110, 2001.

[15] D. S. Bernstein, L. D. Davis, and D. C. Hyland, "The optimal projection equations for reduced-order discrete-time modeling, estimation and control," *Journal of Guidance, Control, and Dynamics*, vol. 9, no. 3, pp. 288–293, 1986.

[16] J. Roskam, *Airplane Design Part 6, Preliminary Calculation of Aerodynamic, Thrust and Power Characteristics*, Roskam Aviation and Engineering Corporation, Ottawa, Kan, USA, 1990.

[17] J. Roskam, *Flight Dynamics Part 4*, Roskam Aviation and Engineering Corporation, Ottawa, Kan, USA, 1971.

[18] "Errata on Jan Roskam, airplane Design Part VI, and Revised August 12, 2003".

[19] U.S. Military Handbook MIL-HDBK-1797, 19, 1997.

[20] B. L. Stevens and F. Lewis, *Aircraft Control and Simulation*, Wiley Interscience Publications, New York, NY, USA, 1992.

[21] H. Kwakernaak, "Robust control and H_∞-optimization—tutorial paper," *Automatica*, vol. 29, no. 2, pp. 255–273, 1993.

[22] G. J. Balas and J. C. Doyle, "Robustness and performance tradeoffs in control design for flexible structures," in *Proceedings of the 29th IEEE Conference on Decision and Control*, vol. 6, pp. 2999–3010, Honolulu, Hawaii, December 1990.

[23] J. Hu, C. Bohn, and H. R. Wu, "Systematic H_∞ weighting function selection and its application to the real-time control of a vertical take-off aircraft," *Control Engineering Practice*, vol. 8, no. 8, pp. 241–252, 2000.

[24] E. Feron, A. Pierre, and G. Pascal, "Analysis and synthesis of robust control systems via parameter-dependent Lyapunov functions," *IEEE Transactions on Automatic Control*, vol. 41, no. 7, pp. 1041–1046, 1996.

[25] G. Pascal, N. Arkadi, J. L. Alan, and C. Mahmoud, *LMI Control Toolbox, for Use with MATLAB*, Mathworks, 1995.